Article

The Structure-Dependent Dynamic Performance of a Twin-Ball-Screw Drive Mechanism via a Receptance Coupling Approach

Uwayezu Marie Chantal [1,2,†], Hong Lu [1,†], Qi Liu [1,*], Tao Jiang [1], Jiji He [1], Shuaiwei Gu [1] and Gashema Gaspard [3]

[1] School of Mechanical and Electronic Engineering, Wuhan University of Technology, Wuhan 430070, China; 410661@whut.edu.cn (U.M.C.); landzh@whut.edu.cn (H.L.); jiangtao283638@whut.edu.cn (T.J.); 283611@whut.edu.cn (J.H.); a18437912875@whut.edu.cn (S.G.)

[2] Department of Mechanical Engineering, Rwanda Polytechnic/Integrated Polytechnic and Regional College-Ngoma (RP/IPRC-Ngoma), Birenga P.O. Box 35, Rwanda

[3] Department of Business Information Technology, University of Rwanda, Kigali P.O. Box 4285, Rwanda; ggas06@yahoo.fr

[*] Correspondence: liunuli@whut.edu.cn

[†] These authors contributed equally to the study.

Abstract: The drive at the center of gravity (DCG) concept-based twin-ball-screw drive mechanism (TBSDM) is vital in automated factories for its robustness and reliability. However, changes in the worktable mass or position result in changes in the center of gravity (CG), significantly affecting the system's dynamic properties. In this regard, this paper introduces a novel analytical model using improved receptance coupling to analyze vibrations in four modes. A mathematical framework for the twin TBSDM is generated, and the effect of changing the worktable position–mass on each mode is examined. The applicability of the proposed method is verified based on dynamic experiments that were carried out on a TBSDM of a CNC grinding wheel machine tool. After thoroughly analyzing the experimental and theoretical results, it is revealed that changing the worktable position primarily influences the rotational and axial vibrations of the twin ball screw (TBS). Furthermore, changes in the worktable mass significantly affect the coupling vibration among the TBSs and rotors or bearings. Moreover, in terms of performance, the variances between the theoretical and experimental natural frequencies are consistently below 5%. Thus, the proposed method is promising for the improvement of the modeling and analysis of the TBSDM.

Keywords: structure-dependent dynamic characteristics; twin-ball-screw feed mechanism; receptance coupling; general dynamic model

1. Introduction

The twin-ball-screw drive mechanism (TBSDM) of a gantry-type computer numerical control (CNC) machine tool is essential to the overall structure. Its reliable dynamic qualities significantly affect the control effectiveness [1–5]. The precise functioning and maintenance of the TBSDM are crucial for obtaining and sustaining high levels of precision. Understanding and optimizing these dynamic properties is paramount to guaranteeing efficient operation. Hence, it mitigates the adverse impacts of vibrations, resonances, and other metrics that may weaken the efficiency [6–9].

Various methods, such as lumped parameters, finite elements, and hybrid approaches, have been employed by different researchers to analyze the dynamic behaviors of the TBSDM [10–13]. Liu Qi et al. [14] adopted the lumped-parameter technique to create a thorough dynamic model of the TBSDM by considering the contact stiffness of kinematic joints. It has been found that the inherent frequency of the TBSDM is greater during motion than when it is static. Its behavior is influenced by the feed rates and locations of its

moving parts. In addition, stability in the TBSDM can be achieved by precisely placing the mobile components at the midpoint of the crossbeam. Duan et al. [15] introduced the lumped-parameter method to create an equivalent model of the TBSDM. They subsequently constructed a finite element model to evaluate its dynamic properties over joint stiffness. Dong et al. [16] analyzed the dynamic features of a ball screw treated as Timoshenko's beam and used the hybrid model approach. They considered flexural, torsional, and axial dynamics. Parameters such as the mass, position, and preload of the table that affect the dynamics of the ball screw were concurrently examined. The proposed methods have several drawbacks since they do not precisely depict the structures of ball screws. Recent research has extensively used a rigid–flexible coupling model that integrates the benefits of the three approaches outlined above to enhance the modeling and analysis of the dynamic performance of the TBSDM [17,18]. Moreover, modal shape analysis has been proposed by several researchers as a traditional method to study the vibrational modes of a TBS structure and the corresponding natural frequencies. Min Hu et al. [5] adopted the model shape technique to investigate the structural dynamics of the dual-driven gantry-type CNC machine tool. The presence of many peaks in the structural frequency response function (FRF) spectrum was the preliminary factor in modal analysis.

The research currently shows that determining the form of vibration that occurs in the ball screw's torsional–axial vibration is challenging due to its slender shaft [19–21]. Nevertheless, the modal shape curve for axial and torsional vibrations could be more evident than for transverse vibrations. The aforementioned studies all used global techniques primarily focused on the high-order dynamic modeling of the TBSDM rather than providing an efficient approach for position-dependent dynamical modeling and evaluation. A notable characteristic is that the entire process of modeling and analyzing the dynamics needs to be performed when the system is placed in a different position or configuration. Hence, they cannot provide a parameterized or explicit function expression of the dynamics that depend on position. Subsequently, the receptance coupling substructuring method for dynamic analysis was proposed to address this issue. This method is based on dividing the equipment into distinct segments to examine the dynamic behaviors of the feed system of the CNC machine tool. It also possesses the necessary position- or mass-dependent dynamic modeling and analysis characteristics [22–26]. In this regard, Ji et al. [27] introduced a novel receptance coupling substructure analysis methodology for predicting the dynamics of the tooltip when a new tool was chosen. However, their investigation ignored the dynamic behaviors of the ball screw feed mechanism, a critical factor influencing the machine tool dynamic system. To develop a mathematical model for the twin-axis feed drive system (FDS), Liu et al. [28] adopted the receptance coupling method. In their model, the worktable was considered rigid, resulting in the absence of a frequency response function (FRF) for this component. The model structure comprised the worktable, carriage, and joint with the FDS model created by coupling the FRF. However, due to the complexity of the proposed model, obtaining the FRF for the worktable was not feasible. Tian et al. [29] analyzed the dynamic properties of a ball screw FDS using a substructure division approach based on its assembly states and structural characteristics. While their findings provided a conceptual framework for improving the dynamic characteristics of ball screw FDSs, their proposed idea focused on a single drive feed system, which does not apply to the TBSFM gantry-type CNC machine tool. Hence, to address the aforementioned limitation, our research introduces an innovative substructure division approach to analyze the vibration of the TBSDM following the drive of the center of gravity (DCG) concept. This method aims to enhance the modeling and analysis of the TBSDM of gantry-type CNC machine tools.

To achieve our research objective, we divided the TBSDM of the CNC grinding wheel machine into several segments. The simulation was conducted with a lumped-parameter method under four critical modes along each X-axis (X_1, X_2). We subsequently developed a mathematical model based on the FRF matrix of each segment with the theoretical results obtained from this model. Additionally, the experimental FRF values were obtained from

vibration tests on the TBSDM of the CNC grinding wheel machine tool, thereby validating our theoretical findings. Thus, in summary, the contributions of this paper are as follows:

1. A substructure division approach to the general modeling of the dynamic characteristics of the drive at the center of gravity (DCG) concept-based TBSFM is presented. The theoretical results, demonstrated through lumped-parameter methods, outline its mathematical framework.
2. The impact of changing the worktable position–mass has been analyzed in four modes to confidently identify the highly affected part of the TBSDM.

The rest of this paper is organized as follows: In Section 2, after introducing the general structure of the TBSDM through the lumped-parameter method, the mathematical equation of FRF matrices is derived and explained using the receptance coupling approach. Section 3 covers the experimental process of evaluating the dynamic properties of the TBSDM. The effects of different factors, such as a change in mass, a change in position, and the two factors combined, on the TBSDM dynamic properties are described in Section 4. Finally, the conclusion of this research and future directions are outlined in Section 5.

2. Modeling of the Twin-Ball-Screw Drive Mechanism

Figure 1 illustrates the twin-ball-screw drive mechanism (TBSDM) structure, showing the 2D design in (a) and the 3D design in (b), which were examined for their high-speed and precision capabilities. The dual-driven construction in the *X*- and *Y*-directions significantly enhances transmission stiffness in both feed directions. However, this study focuses on the *X*-direction as a case study. However, the conventional structure includes two servomotors, two ball screws, two linear guide rails, bearings, a worktable, and other components. It is well noted that the primary focus of TBSDM research is the accuracy of the worktable's axial feed, as the axial and torsional vibrations of the two ball screws (along the X_1–X_2-axis) significantly impact the worktable's axial vibration.
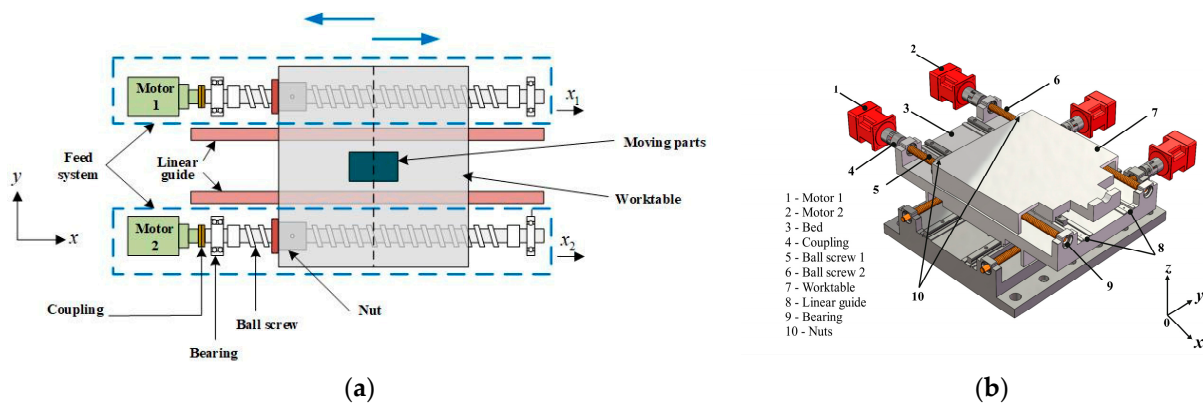

Figure 1. The general structure of the TBDM: (**a**) 2D structure design, (**b**) 3D model designed in solidworks 2023 Software.

Figure 2 illustrates the fundamental model of the twin-ball-screw drive mechanism (TBSDM), with a specific focus on the axial and torsional vibrations of the screws, as well as the axial vibration of the worktable. The labels k_{a1l}-k_{a2l} refer to the axial stiffness along the X_1- and X_2-axes on the left side, respectively, while the labels k_{a1r}-k_{a2r} denote the axial stiffness on the right side. Similarly, c_{a1l}-c_{a2l} and c_{a1r}-c_{a2r} denote the axial damping along X_1 and X_2 on the left and right sides, respectively. Furthermore, k_{m1}-k_{m2} and c_{m1}-c_{m2} represent the torsional stiffness and damping of the coupling ball-screw–motor along X_1 and X_2, respectively, reflecting the rotational angle along X_1 and X_2. Additionally, k_{n1}-k_{n2} and c_{n1}-c_{n2} indicate the stiffness of the screw–nut joint with their corresponding damping for X_1 and X_2 shafts, respectively. X_b denotes the axial vibration of the worktable, while ϕ_1'ϕ_2 present the rotational vibration of the first and second ball screws, respectively.
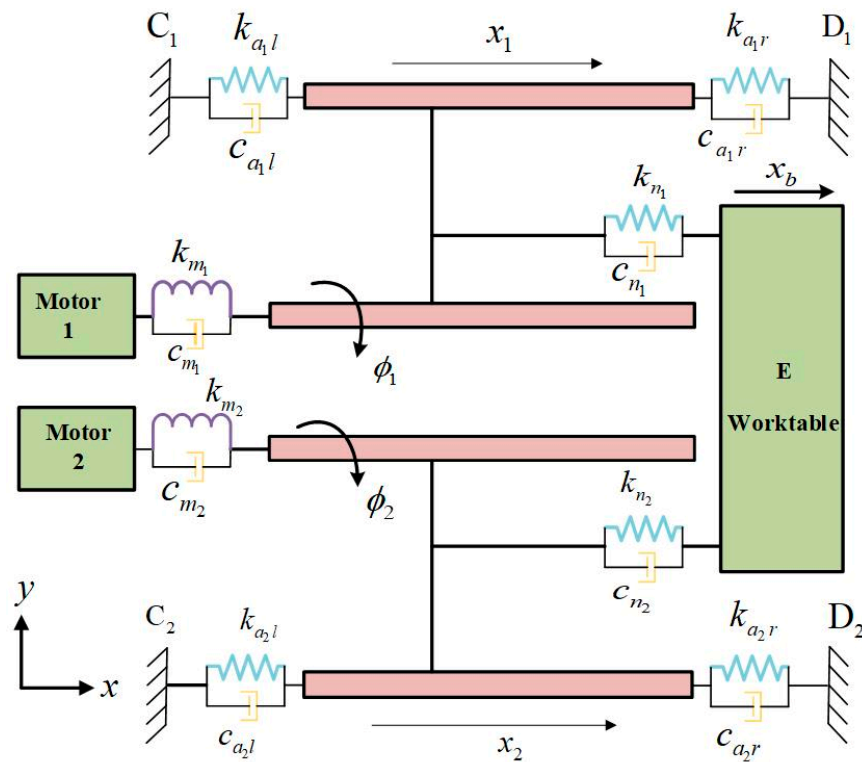
Figure 2. Simplified TBSDM model.

2.1. Modeling of the Twin-Ball-Screw Drive Mechanism

This study presents a new substructure division approach based on applying a lumped-parameter model to the twin-ball-screw drive mechanism (TBSDM). This approach aims to solve the limitation of the current receptance coupling method, which fails to simulate the worktable TBSDM. The worktable's frequency response function (FRF) can be determined by analyzing the substructure's FRF, which consists of a portion of the TBSs as well as the worktable.

The two ball screws (BSs) are divided into segments (4 for each ball screw), A_1-B_1-H_1-F_1 and A_2-B_2-H_2-F_2, as shown in Figure 3. Segments F_1-F_2 represent the sections that touch the coupling BS and nut 1–nut 2, while H_1-H_2 describe the contact parts of the coupling BS–motor concerning the X_1-axis for the first motor and X_2-axis for the second motor, respectively. The segments of BSs between F_1-H_1 and F_2-H_2 are segments A_1 and A_2, while the rest cover segments B_1 and B_2. The eight segments presented above are rigidly connected; therefore, the lumped-parameter model was adopted to simulate segments A_1-B_1 and A_2-B_2 of two ball screws. The axial substructure encompasses the axial models of the ball screws (A_1-B_1, A_2-B_2) and the bearing components. The torsional substructure consists of the torsional models of the coupling A_1-B_1-H_1 and A_2-B_2-H_2, as well as the rotors. The worktable substructure comprises the axial–torsional models of F_1-F_2 and the worktable. The FRFs of the substructure can easily be derived using the finite element method (FEM). In modeling the feed drive mechanism, the FRFs of the axial–torsional substructures are independently coupled with segments F_1 and F_2, utilizing a similar degree of freedom.
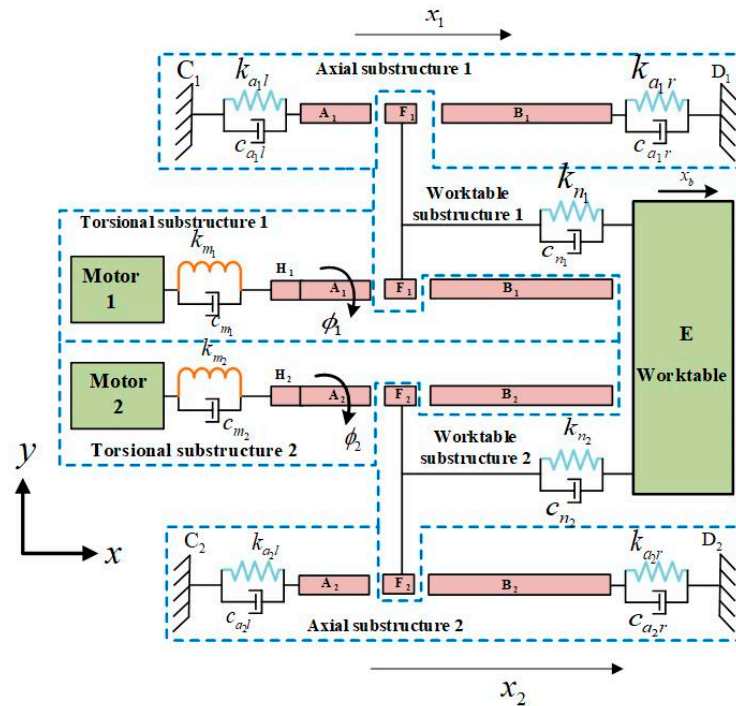
Figure 3. A schematic illustration of the substructures of the TBSDM.

2.2. Establishment of TBSDM Axial Substructure

Figure 4 depicts the axial substructure model of a TBSDM. Points 1 to 4 are considered the designated locations for excitation and response to represent the FRF of the substructure. Furthermore, l_1 and l_2 denote the respective lengths of A_1 and A_2, while L_1 and L_2 represent the total lengths of the two different ball screws. Recall that l_1 is equal to l_2 and l. In addition, L_1 is equal to L_2 as well as L.
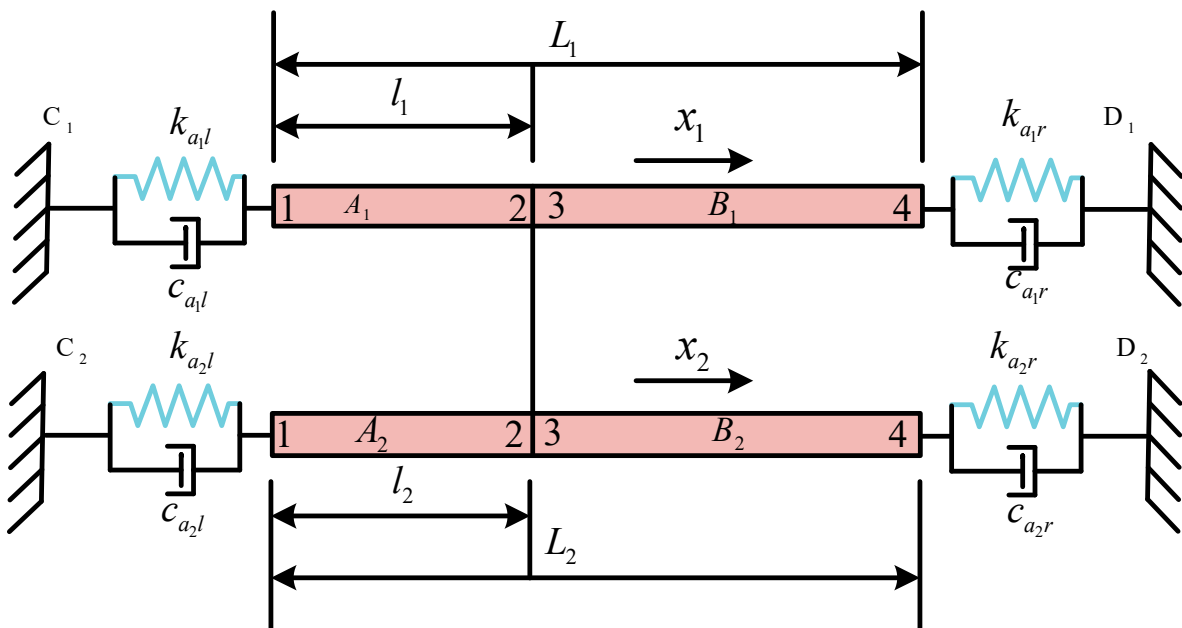

Figure 4. A schematic depiction of the twin ball screws' axial substructures.

2.2.1. TBS's Axial Vibration Condition

Euler–Bernoulli (EB) beams were utilized to model the axial vibration of the twin ball screw in this paper. Following Figure 4, segments A_1, A_2, B_1, and B_2 are modeled as circular shafts with unconstrained ends. However, the axial FRF matrix could be determined by applying the following equations [30,31].

Since segments A_1-B_1 represent the axial condition of a single ball screw along the X_1-axis for motor 1, based on EB beams, their corresponding FRF matrix (F_{A1-a} (l_1)-F_{B1-a} (l_1)) can be obtained in Equations (1) and (2).

$$F_{A_1-a}(l_1) = \begin{bmatrix} f_{A_1-a_{11}}(l_1) & f_{A_1-a_{12}}(l_1) \\ f_{A_1-a_{21}}(l_1) & f_{A_1-a_{22}}(l_1) \end{bmatrix} = (E_1 S_1 \beta_1)^{-1} \begin{bmatrix} -\cos(\beta_1 l_1) & -\csc(\beta_1 l_1) \\ -\csc(\beta_1 l_1) & -\cos(\beta_1 l_1) \end{bmatrix} \tag{1}$$

$$F_{B_1-a}(l) = \begin{bmatrix} f_{B_1-a_{33}}(L-l_1) & f_{B_1-a_{34}}(L-l_1) \\ f_{B_1-a_{43}}(L-l_1) & f_{B_1-a_{44}}(L-l_1) \end{bmatrix} = (E_1 S_1 \beta_1)^{-1} \begin{bmatrix} -\cos\beta_1(L-l_1) & -\csc\beta_1(L-l_1) \\ -\csc\beta_1(L-l_1) & -\cos\beta_1(L-l_1) \end{bmatrix} \tag{2}$$

Segments A_2-B_2 in Figure 4 describe the axial condition of the ball screw along the X_2-axis for motor 2. Since the proposed model has a symmetric condition, the FRF matrix (F_{A2-a} (l_2)-F_{B2-a} (l_2)) along the X_2-axis for motor 2 can also be derived following Equations (1) and (2), wherein the labels with index (1) in Equations (1) and (2) will be replaced by labels with index (2).

In addition, the labels A_1-B_1 and A_2-B_2 denote the ball screw substructures, while the symbol a represents the axial FRF. The labels F_{A1-a} (l_1) and F_{A2-a} (l_2) are the axial FRF matrices for segments A_1 and A_2. The label f_{A-a12} (l) stands for the axial FRF with the response at point 1 and excitation at point 2, E_1 and E_2 are the elasticity moduli of the two ball screws, S_1 and S_2 are their cross-sectional areas, ω is the angular frequency, and ρ represents the TBS density. The two ball screws in the proposed drive mechanism are considered symmetric models; therefore, the FRF matrices along X_1 and X_2 are equal. Since $\beta = \beta_1 = \beta_2$ and can be calculated based on Equation (3), $E_1 = E_2 = E$, $S_1 = S_2 = S$, and $l_1 = l_2 = l$, as well as $L_1 = L_2 = L$.

Considering that the connection between A_1-B_1 and A_2-B_2 depicts a rigid coupling, based on the receptance coupling method, the disassembled FRF matrices F_{A1B1-a} for the X_1-axis and F_{A2B2-a} for X_2 can be generated by linking segments A_1-B_1 and A_2-B_2, as presented in Equations (3) and (4).

$$\beta = \omega \sqrt{\frac{\rho}{E}} \tag{3}$$

$$
F_{A_1B_1-a}(l_1) = \begin{bmatrix} f_{A_1B_1-a11}(l) & f_{A_1B_1-a12}(l) & f_{A_1B_1-a14}(l) \\ f_{A_1B_1-a21}(l) & f_{A_1B_1-a22}(l) & f_{A_1B_1-a24}(l) \\ f_{A_1B_1-a41}(l) & f_{A_1B_1-a42}(l) & f_{A_1B_1-a44}(l) \end{bmatrix} =
$$
$$
\begin{bmatrix} f_{A_1-a11}(l) & f_{A_1-a12}(l) & 0 \\ f_{A_1-a21}(l) & f_{A_1-a22}(l) & 0 \\ 0 & 0 & f_{B_1-a44}(l_1) \end{bmatrix} + \begin{bmatrix} f_{A_1-a12}(l) \\ f_{A_1-a22}(l) \\ f_{A_1-a43}(l) \end{bmatrix} \left[f_{A_1-a22}(l) + f_{B_1-a33}(l) \right]^{-1} \begin{bmatrix} f_{A_1-a21}(l) \\ f_{A_1-a22}(l) \\ f_{B_1-a34}(l) \end{bmatrix}^T \tag{4}
$$

$$
F_{A_2B_2-a}(l_2) = \begin{bmatrix} f_{A_2B_2-a11}(l) & f_{A_2B_2-a12}(l) & f_{A_2B_2-a14}(l) \\ f_{A_2B_2-a21}(l) & f_{A_2B_2-a22}(l) & f_{A_2B_2-a24}(l) \\ f_{A_2B_2-a41}(l) & f_{A_2B_2-a42}(l) & f_{A_2B_2-a44}(l) \end{bmatrix} =
$$
$$
\begin{bmatrix} f_{A_2-a11}(l) & f_{A_2-a12}(l) & 0 \\ f_{A_2-a21}(l) & f_{A_2-a22}(l) & 0 \\ 0 & 0 & f_{B_1-a44}(l) \end{bmatrix} + \begin{bmatrix} f_{A_2-a12}(l) \\ f_{A_2-a22}(l) \\ f_{A_2-a43}(l) \end{bmatrix} \left[f_{A_2-a22}(l) + f_{B_2-a33}(l) \right]^{-1} \begin{bmatrix} f_{A_2-a21}(l) \\ f_{A_2-a22}(l) \\ f_{B_2-a34}(l) \end{bmatrix}^T \tag{5}
$$

2.2.2. The Axial Vibration Condition between the TBS and the Bearing

Figure 4 describes the overall structure of axial vibration in the coupling ball-screw–bearing. Let us consider beds C_1-C_2 a rigid body fixed on the ground. Their axial FRFs will automatically be zero, which means that f_{c1-a} is equal to f_{c2-a}, and both are zero. The labels are f_{J2-al} and $f_{J2-al}l$, which denote the FRFs for the connection between the first ball screws and point C_1 and the second ball screw and point C_2, respectively.

$$f_{J_1-al} = f_{J_2-al} = f_{J-al} = k_{al} + iwcl \tag{6}$$

However, the axial frequency between points A_1-C_1 and A_2-C_2, denoted by F_{A1C1-a} (l_1) and F_{A2C2-a} (l_2), can be obtained by connecting the FRF matrix of the joints between the ball screw and segment A_1-A_2 as well points C_1-C_2, as described in Equation (7).

$$
F_{A_1C_1-a}(l_1) = \begin{bmatrix} f_{A_1C_1-a11}(l) & f_{A_1C_1-a12}(l) & f_{A_1C_1-a14}(l) \\ f_{A_1C_1-a21}(l) & f_{A_1C_1-a22}(l) & f_{AC_1-a24}(l) \\ f_{A_1C_1-a41}(l) & f_{A_1C_1-a42}(l) & f_{A_1C_1-a44}(l) \end{bmatrix} =
$$
$$
F_{A_1B_1-a}(l_1) + \begin{bmatrix} f_{A_1B_1-a11}(l) \\ f_{A_1B_1-a21}(l) \\ f_{A_1B_1-a41}(l) \end{bmatrix} \left[f_{A_1B_1-a11}(l) + f_{J_1-al_1} + f_{c_1-a} \right]^{-1} \begin{bmatrix} f_{A_1B_1-a11}(l) \\ f_{A_1B_1-a12}(l) \\ f_{A_1B_1-a14}(l) \end{bmatrix}^T \tag{7}
$$

The FRF matrix along segment AD can be obtained by applying the same method used for AC since D1 and D2 represent the beds, as shown in Equation (8).

$$
F_{A_1D_1-a}(l_1) = \begin{bmatrix} f_{A_1D_1-a11}(l) & f_{A_1D_1-a12}(l) & f_{A_1D_1-a14}(l) \\ f_{A_1D_1-a21}(l) & f_{A_1D_1-a22}(l) & f_{A_1D_1-a24}(l) \\ f_{A_1D_1-a41}(l) & f_{A_1D_1-a42}(l) & f_{A_1D_1-a44}(l) \end{bmatrix} =
$$
$$
F_{A_1C_1-a}(l_1) + \begin{bmatrix} f_{A_1C_1-a11}(l) \\ f_{A_1C_1-a21}(l) \\ f_{A_1C_1-a41}(l) \end{bmatrix} \left[f_{A_1C_1-a11}(l) + f_{J-al} + f_{c_1-a} \right]^{-1} \begin{bmatrix} f_{A_1C_1-a11}(l) \\ f_{A_1C_1-a12}(l) \\ f_{A_1C_1-a14}(l) \end{bmatrix}^T \tag{8}
$$

2.3. Establishment of TBSDM Rotational Substructure

The torsional substructure model of the twin-ball-screw drive mechanism (TBSDM) is illustrated in Figure 5. The two-ball-screw model is considered symmetric in this paper; therefore, position l_1 is equal to l_2 and can be replaced by l, and L_1 is equal to L_2 and can be replaced by L.
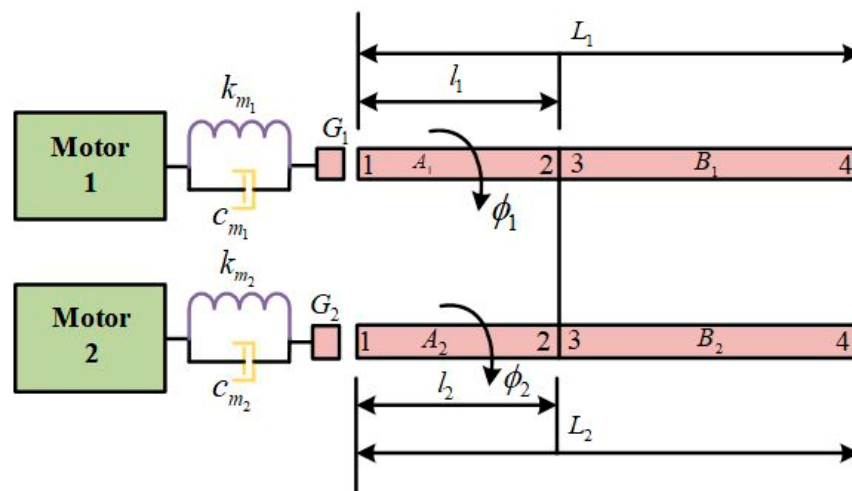

Figure 5. The torsional substructure model of the TBSDM.

2.3.1. The Torsional Vibration Condition of Ball Screws

As described in Figure 5, segments A_1-B_1 and A_2-B_2 of the two ball screws (BSs) are circular shafts with free ends. However, their corresponding torsional FRF matrix was obtained following the Euler–Bernoulli (EB) beam theory. The labels F_{A1-t}, F_{A2-t}, F_{B1-t}, and F_{B2-t} represent the torsional FRFs at points A_1-B_1 for the first motor and A_2-B_2 for the second motor, respectively, t indicates the torsional FRF, G_1-G_2 are the shear elasticities of the BSs, and $\beta = \beta_1 = \beta_2$ can be calculated based on Equation (3).

Considering the first motor, the torsional vibrations of the BSs are denoted by F_{A1-t} at point A1 and F_{B1-t} at point B_1 and can be derived in Equations (9) and (10).

$$F_{A_1-t}(l_1) = \begin{bmatrix} f_{A_1-t_{11}}(l_1) & f_{A_1-t_{12}}(l_1) \\ f_{A_1-t_{21}}(l_1) & f_{A_1-t_{22}}(l_1) \end{bmatrix} = (G_1 J_1 \beta_1)^{-1} \begin{bmatrix} -\cot(\beta_1 l_1) & -\csc(\beta_1 l_1) \\ -\csc(\beta_1 l_1) & -\cot(\beta_1 l_1) \end{bmatrix} \tag{9}$$

$$F_{B_1-t}(l_1) = \begin{bmatrix} f_{B_1-t_{11}}(L_1 - l_1) & f_{B_1-t_{12}}(L_1 - l_1) \\ f_{B_1-t_{21}}(L_1 - l_1) & f_{B_1-t_{22}}(L_1 - l_1) \end{bmatrix} = (G_1 J_1 \beta_1)^{-1} \begin{bmatrix} -\cot(\beta_1(L_1 - l_1)) & -\csc(\beta_1(L_1 - l_1)) \\ -\csc(\beta_1(L_1 - l_1)) & -\cot(\beta_1(L_1 - l_1)) \end{bmatrix} \tag{10}$$

Consequently, since two ball screws possess the symmetric condition, the torsional FRF matrices of ball screws at point A2 (F_{A2-t}) and point B2 (F_{B2-t}) along motor 2 can also be computed using Equations (11) and (12).

Therefore, the torsional vibration of the entire BS (F_{A1B1-t} and F_{A2B2-t}) is obtained by connecting the FRF matrix in segments A1-B1 for the first motor and A2-B2 for the second motor. Moreover, the optimal value of the torsional vibration of the two ball screws can be obtained in Equation (14). Note that the labels $J1$ and $J2$ are represented in Equation (11), where d stands for the diameters of the BSs.

$$J_1 = J_2 = \frac{\pi d^4}{32} \tag{11}$$

$$F_{A_1B_1-t}(l_1) = \begin{bmatrix} f_{A_1B_1-t11}(l) & f_{A_1B_1-t12}(l) & f_{A_1B_1-t14}(l) \\ f_{A_1B_1-t21}(l) & f_{A_1B_1-t22}(l) & f_{A_1B_1-t24}(l) \\ f_{A_1B_1-t41}(l) & f_{A_1B_1-t42}(l) & f_{A_1B_1-t44}(l) \end{bmatrix} =$$
$$\begin{bmatrix} f_{A_1-t11}(l) & f_{A_1-t12}(l) & 0 \\ f_{A_1-t21}(l) & f_{A_1-t22}(l) & 0 \\ 0 & 0 & f_{B_1-t44}(l_1) \end{bmatrix} + \begin{bmatrix} f_{A_1-t12}(l) \\ f_{A_1-t22}(l) \\ f_{A_1-t43}(l) \end{bmatrix} \left[f_{A_1-t22}(l_1) + f_{B_1-t33}(l) \right]^{-1} \begin{bmatrix} f_{A_1-t21}(l) \\ f_{A_1-t22}(l) \\ f_{B_1-t34}(l) \end{bmatrix}^T \tag{12}$$

The labels with index (1) in Equation (12) will be replaced by labels with index (2) to obtain the FRF matrix of connection A_2-B_2 (F_{A2B2-t}).

2.3.2. The Torsional Vibration Condition between the Ball Screws and Motors

The rotating elements of the rotors and parts H_1-H_2 of the ball screws are linked via a coupling, as depicted in Figure 5. The mass matrix, stiffness matrix, and damping matrix, denoted by M_H, K_H, and C_H, respectively, are derived based on the finite element method, as shown in the following Equations (13)–(15), and their corresponding value are summarized in Table 1.

$$M_H = \begin{bmatrix} J_m & 0 \\ 0 & J_{sH} \end{bmatrix} \tag{13}$$

$$K_H = \begin{bmatrix} k_m & -k_m \\ -k_m & k_m \end{bmatrix} \tag{14}$$

$$C_H = \begin{bmatrix} c_m & c_m \\ -c_m & c_m \end{bmatrix} \tag{15}$$

Table 1. Specifications and parameters of TBSDM with their corresponding values.

Component	Parameter	Symbol	Value	Unit
Ball screw	Elasticity modulus	E	2.06×10^5	MPa
	Shear elasticity	G	7.92×10^4	MPa
	Density	ρ	7.89×10^3	kg/m^3
	Diameter	d	0.02	m
	Inertia of segment (F)	J_s	1×10^{-4}	kg/m^2
	Inertia of segment (H)	J_{sH}	1×10^{-4}	kg/m^2
	The inertia of the rotor	J_m	1.67	kg/m^2
	Axial stiffness	k_n	7.017×10^7	N/m
	Mass	m	7.61	kg
	Angular frequency	ω	2	rad/s
	Total length	L	0.150	m
Bearing	Axial damping in the left bearing group	c_{al}	2.02×10^3	Ns/m
	Axial stiffness in the left bearing group	k_{al}	7.229×10^7	N/m
	Axial stiffness in the right bearing group	k_{ar}	7.229×10^7	N/m
	Axial damping in the right bearing group	c_{ar}	2.94×10^7	Ns/m
Coupling	Torsional stiffness	k_m	1.75×10^5	Nm * s/rad.
	Torsional damping	c_m	3.50	Ns/m

J_m is equal to Jm_1 for motor 1 and Jm_2 for the second motor and represents the inertia of the rotors. The labels J_{sH1}-J_{sH2} are equal to J_{sH} and stand for the inertia of parts H$_1$-H$_2$, which are the connections rotor 1–ball screw 1 and rotor 2–screw 2, respectively, and the FRF in this section is denoted by f_{H1-t00}-f_{H2-t00} and is calculated by adopting the equation of motion provided by Lagrange theory, as developed in [15].

Assume that the connection between A$_1$-H$_1$ and A$_2$-H$_2$ represents a rigid body coupling; the FRF of the torsional substructure will be derived by connecting the rotating elements of the two motors (H$_1$-H$_2$) with their related parts of the ball screws (A$_1$-A$_2$). Therefore, the rotational vibration of the ball-screw–motor can be expressed as F$_{A1H1-t}$ for the first motor and F$_{A2H2-t}$ for the second motor; thus, it will be calculated as follows in Equations (16) and (17):

$$F_{A_1 H_1 - t}(l_1) = \begin{bmatrix} f_{A_1 H_1 - t11}(l) & f_{A_1 H_1 - t12}(l) & f_{A_1 H_1 - t14}(l) \\ f_{A_1 H_1 - t21}(l) & f_{A_1 H_1 - t22}(l) & f_{A_1 H_1 - t24}(l) \\ f_{A_1 H_1 - t41}(l) & f_{A_1 H_1 - t42}(l) & f_{A_1 H_1 - t44}(l) \end{bmatrix} = F_{A_1 B_1 - t}(l_1) + \begin{bmatrix} -f_{A_1 B_1 - t11}(l) \\ f_{A_1 B_1 - t21}(l) \\ f_{A_1 B_1 - t41}(l) \end{bmatrix} \left[f_{A_1 B_1 - t22}(l) + f_{H_1 - t00}(l) \right]^{-1} \begin{bmatrix} f_{A_1 B_1 - a11}(l) \\ f_{A_1 B_1 - a12}(l) \\ f_{A_1 B_1 - a14}(l) \end{bmatrix}^T \tag{16}$$

$$F_{A_2 H_2 - t}(l_1) = \begin{bmatrix} f_{A_2 H_2 - t11}(l) & f_{A_2 H_2 - t12}(l) & f_{A_2 H_2 - t14}(l) \\ f_{A_2 H_2 - t21}(l) & f_{A_1 H_1 - t22}(l) & f_{A_2 H_2 - t24}(l) \\ f_{A_2 H_2 - t41}(l) & f_{A_2 H_2 - t42}(l) & f_{A_2 H_2 - t44}(l) \end{bmatrix} = F_{A_2 B_2 - t}(l_1) + \begin{bmatrix} -f_{A_2 B_2 - t11}(l) \\ f_{A_2 B_2 - t21}(l) \\ f_{A_2 B_2 - t41}(ll_1) \end{bmatrix} \left[f_{A_2 B_2 - t22}(l) + f_{H_2 - t00}(l) \right]^{-1} \begin{bmatrix} f_{A_2 B_2 - a11}(l) \\ f_{A_2 B_2 - a12}(l) \\ f_{A_2 B_2 - a14}(l) \end{bmatrix}^T \tag{17}$$

The above mathematical models were manipulated in math lab software to predict the effect of changing the worktable position or mass on the axial vibration of the ball screws themselves (Equations (4) and (5)). For the axial vibration of the coupling ball-screw–bearing, Equations (7) and (8) are used; for the rotational vibration of the ball screw alone, Equations (9) and (10) are used, and for that between motors and ball screws, Equations (16) and (17) are used. The optimal value of the predicted natural frequency obtained mathematically for each mode has been compared to the experimental result. Table 1 outlines the parameters used in the modeling process, which were either obtained from the manufacturers' catalogs; approximated from prior research; or calculated from computer-aided design (CAD) models of the TBSDM components shown in Figure 1b. Moreover, the mathematical model determines the theoretical value of the TBSDM natural frequency.

3. Experimental Analysis of Dynamics

This section validates the precision of the model proposed in this work by comparing empirical test data with model analysis data. The experimental setup of the TBSD mechanism is demonstrated in Figure 6. The model test was conducted on the TBSDM of the CNC grinding wheel machine tool developed by Wuhan University of Technology's lab, and it uses the Beckhoff control system. The model has four permanent-magnetic synchronous motors (PMSM-AM8531), two for the X-direction and another two for the Y-direction, but our research considers the X-direction only. The DYTRAN (5800B5) impulse force hammer and acceleration sensors (model: BK4507B) were employed for experiments using the single-point excitation multi-point vibration pickup approach. Ten acceleration sensors with fourteen directions were used to analyze the vibration in different substructures.
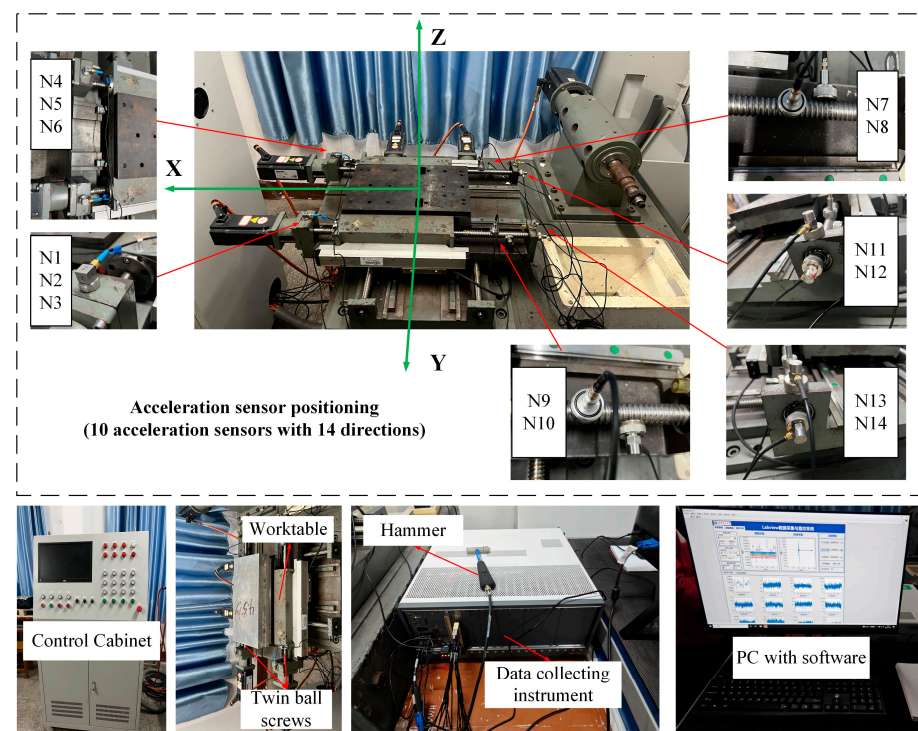

Figure 6. Experimental setup of the TBSD mechanism.

The sensors' arrangement in our experiment is described as follows: The axial vibration of the two ball screws (mode 1) was captured by sensors N1-N4, and the rotational vibration in the coupling ball-screws–motors (mode 4) was detected by sensors N2-N3 and N5-N6. The rotational vibration of the ball screws themselves (mode 3) was captured by using the four unidirectional sensors N7-N8 and N9-N10. Furthermore, the sensors N11-N12 and N1-N14 detected the axial vibration of the coupling ball-screw–bearing (mode 2). Vibration acquisition equipment (pxie4499) developed by a national instrument company (NI) was used to collect high-precision data, and the data processing was carried out by the lab-viewer application.

The frequency response curve was obtained through curve fitting by applying the fast Fourier transform (FFT) method. Since our model has a twin axis, the overall mean value of the natural frequency was considered the optimal value in each mode. Therefore, the experimental value obtained through a modal test is presented in this paper. Since the worktable position significantly impacts the dynamic behavior of the feed drive system (FDS) [28], the study's validity was confirmed by contrasting the model's predictions with experimental data collected at four worktable positions.

To obtain the experimental values shown in Table 2, we settled the dual-driven CNC grinding wheel machine tool into four different positions at the initial mass of 23.5 kg. Our

machine has a total length of 0.150 m; therefore, the first position was $l_1 = 0.02$ m, the second was $l_2 = 0.05$ m, the third was $l_3 = 0.08$, and the last one was $l_4 = 0.11$ mm. We utilized the FFT method to transform the measured data into the frequency domain, and the obtained natural frequency with its corresponding magnitude was recorded. The errors between the measured natural frequencies obtained through the modal test and the ones from the calculation (theoretical values) were determined, and it was shown that the highest value of error in all modes was less than 5%, implying that the model accurately represents the dynamic properties of the TBSDM.

Table 2. The comparison between theoretical and experimental natural frequencies.

Positions (m)		Natural Frequency (Hz)			
		First Mode	Second Mode	Third Mode	Fourth Mode
$l_1 = 0.02$	Experimental	359	386	223	298
	Theoretical	349	383	220	260
	Errors	2.78%	0.77%	1.4%	1.5%
	Magnitude (m/N)	0.14	0.23	0.12	0.49
$l_2 = 0.05$	Experimental	409	400	225	321
	Theoretical	402	401	223	319
	Errors	1.71%	−0.5%	4.4%	1.34%
	Magnitude (m/N)	0.22	0.32	0.08	0.48
$l_3 = 0.08$	Experimental	378	388	222	310
	Theoretical	375	376	219	308
	Errors	0.94%	0.52%	4.41%	0.6%
	Magnitude (m/N)	0.14	3.1	0.1	0.40
$l_4 = 0.110$	Experimental	368	376	220	305
	Theoretical	372	375	219	300
	Errors	−1.1%	0.26%	4.4%	1.6%
	Magnitude (m/N)	0.13	0.2	0.13	0.45

4. Results and Discussion

This part predicts the vibration mode of the twin-ball-screw drive mechanism (TBSDM) by studying the natural frequency distribution in four different coupling conditions. The effects of the worktable position and worktable mass on the dynamic features of the TBDM are evaluated separately in specific subsections. Additionally, the combined impact of these two factors is then analyzed synthetically.

4.1. Impact of Worktable Position on Dynamics of TBSDM

This section describes how the worktable position affects the dynamic properties of the TBSDM. We examined the vibration of the TBSDM in four fundamental modes as follows:

- The mode caused by the axial vibration of the ball screw (first mode).
- The axial vibration of the coupling between the ball screw and the bearing (second mode).
- The torsional vibration between the ball screw and motor (third mode).
- Finally, the torsional vibration of the twin ball screws themselves (fourth mode).

The analysis was conducted theoretically using the specified equations to obtain the FRF matrices of each mode, and the results were experimentally confirmed using a TBSDM of the CNC grinding wheel machine tool. The differences between the theoretical and measured values of natural frequency are integrated in Table 2. In addition, the maximum and minimum natural frequencies of the four modes are summarized in Table 3. The basic concept governing the variations in the natural frequencies of the four modes presented in Figure 7a is that they increase in the central location and are reduced on each side. The worktable is positioned at the center of gravity of the machine tool, and the lengths of the ball screws between the constraint position and both ends are equal. When the worktable

travels toward the right part of the X_1- or X_2-axis, the left ball screw of the worktable extends, while the right ball screw decreases. Consequently, the inherent frequencies of the rotational and axial oscillations of the ball screw drop, indicating a reduction in the frequencies of the first and fourth modes of the associated feed drive system as well. Hence, the fundamental principle (elevated in the center and diminished on both ends) is presented in this part.

Table 3. Impact of worktable position on dynamic properties of TBSDM.

Condition	Natural Frequency (Hz)			
	First Mode	**Second Mode**	**Third Mode**	**Fourth Mode**
Maximum	409	401	225	321
Minimum	372	375	219	298
Variation rate	9.98%	6.9%	2.7%	7.1%
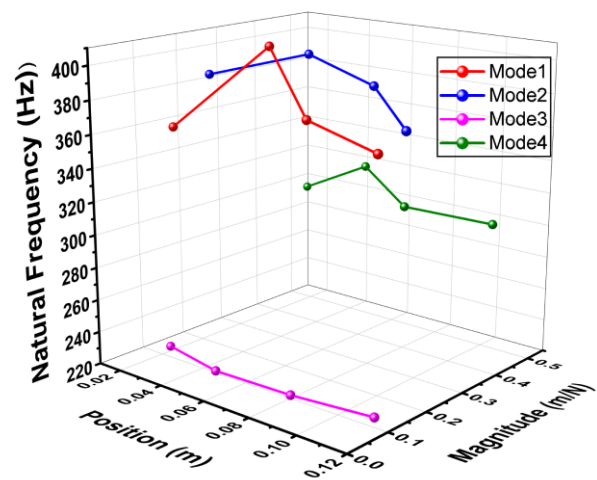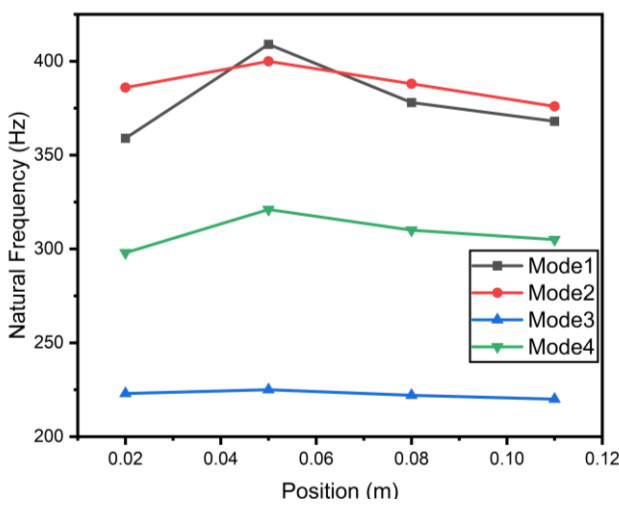
(**a**) (**b**)

Figure 7. Effect of worktable position on dynamic properties of 4 modes: (**a**) position vs. natural frequency, (**b**) position vs. natural frequency with magnitude.

The minimum deformation observed in the curves of the second and third modes proved that changing the worktable position has a negligible impact on the connection between the ball screws and motor bearings. The mode 1 curve, which represents the axial vibration of the two ball screws, exhibits greater deformation in the middle part compared to the mode 4 curve (BS rotational vibration). This is due to the unequal magnitudes of the axial stiffness of the bearings at both ends. The initial mode exhibits a wider range of variation in natural frequency compared to the fourth mode due to the narrow nature of the ball screw shaft, hence its lower torsional stiffness relative to their axial stiffness.

4.2. Impact of Worktable Mass on Dynamics of TBSDM

The worktable mass effect on the dynamic properties of the TBSDM is studied in this part since worktable mass is among the parameters to account for the TBSDM designing process. To determine the influence of worktable mass on the entire system, as shown in Tables 4 and 5, we configured our machine with four different masses at the initial position ($l_1 = 0.002$ m). First, we calculated the natural frequencies in our four modes at the initial worktable mass of M0 = 23.5 kg in the initial position ($l_1 = 0.02$), and secondly, we added three external masses, as shown in Figure 6, to vary the worktable mass. The second worktable mass was M1 = 28 kg, the third one was M2 = 32.5 kg, and the last one was M3 = 37 kg. It is noted that the change in worktable mass was observed at the initial

worktable position $l_1 = 0.002$. The measured natural frequency and its corresponding magnitude were recorded and are plotted in Figure 8. The effect of changing worktable mass on the dynamics of the TBFDM was subsequently analyzed, as shown in Figure 8a, considering the variation in natural frequency vs. the change in mass in all modes. Figure 8b describes the same effect considering each mode's magnitude. It was found that an increase in mass caused a decrease in natural frequency in all modes, but the highest change rate was observed in the curves of mode 2 and mode 3. Figure 8b shows that the increase in mass has a higher magnitude in mode 3 and mode 4 than in the first and second modes. Therefore, this research can confidently conclude that the variation in worktable mass significantly affects the coupling ball-screw–bearing (mode 2) and ball-screw–motor (mode 3) since the change in worktable mass has a negligible effect on the axial (mode 1) and rotational vibrations (mode 4) of the ball screws themselves.

Table 4. Experimental data on the change in natural frequency vs. change in mass for four modes.

Mass (kg)	Natural Frequency (Hz)			
	First Mode	**Second Mode**	**Third Mode**	**Fourth Mode**
M0 = 23.5	388 Magnitude =0.16	302 Magnitude =0.3	225 Magnitude =1.0	316 Magnitude =0.9
M1 = 28	387 Magnitude =0.15	299 Magnitude =0.2	216 Magnitude =0.9	308 Magnitude =0.5
M2 = 32.5	385 Magnitude =0.13	267 Magnitude =0.25	214 Magnitude =0.75	306 Magnitude =0.3
M3 = 37	380 Magnitude =0.1	260 Magnitude =0.2	210 Magnitude =0.6	300 Magnitude =0.6

Table 5. Impact of worktable mass on dynamic properties of TBSDM.

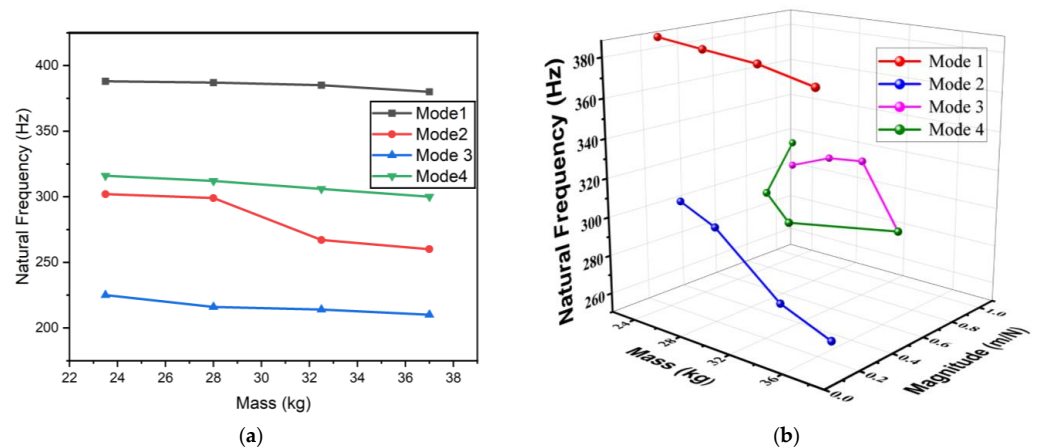| Condition	Natural Frequency (Hz)			
	First Mode	**Second Mode**	**Third Mode**	**Fourth Mode**
Maximum	388	302	225	316
Minimum	380	260	202	300
Variation rate	2.6%	16%	11%	5%

Figure 8. The influence of a change in mass on the natural frequency of the entire system: (**a**) natural frequency vs. mass, (**b**) change in frequency, magnitude, and mass.

4.3. The Impact of Dual Factors on Dynamic Properties of TBSDM

To analyze the effect of two factors (worktable position–mass) on the dynamic properties of the entire TBSDM, we first recorded the natural frequency in each mode at l_1–l_4 with the initial worktable mass M0 = 23.5 kg and then at l_1–l_4 with M0 = 28 kg; the third group was l_1–l_4 with M2 = 32.5 kg, and last was l_1–l_4 with the mass M3 = 37 Kg. To obtain the values in Table 6, we considered the maximum–minimum natural frequency of each model and measured the variation in natural frequency with the increase in the worktable position at a fixed mass (M0-M1-M2-M3). The overall change rate was calculated to show highly affected modes. Thus, as depicted in Figure 9, the curves in mode 1 and mode 4 show that an increase in position increases the natural frequency, especially in the middle area of the machine, while staying stable concerning the variation in mass. An increase in mass decreases the natural frequency in all modes, but the effect is most pronounced in the second and third ones.

Table 6. Effect of dual factors on dynamic properties of TBSDM.

Mass (kg)		Natural Frequency (Hz)			
		Mode 1	**Mode 2**	**Mode 3**	**Mode 4**
M0 = 23.5	Maximum	415	422	225	324.5
	Minimum	409	373	219	303
	Variation rate	1.4%	13%	2.7%	7%
M1 = 28	Maximum	410	373	220	321
	Minimum	395	322	216	297
	Variation rate	3.7%	13.6%	1.85%	8%
M2 = 32.5	Maximum	402	320	218	294
	Minimum	395	294	214.5	281
	Variation rate	1.77%	8.8%	1.6%	4.6%
M3 = 37	Maximum	385	286	216	283
	Minimum	380	277	214	252
	Variation rate	1.3%	3.2%	0.9%	12%
	Overall change rate	2%	9.5%	1.76%	7.75%

The results of this study can be briefly described as follows: When examining the impact of the worktable position on the dynamics of the TBDS, as indicated in Tables 2 and 3, it was discovered that the natural frequencies of the first and fourth modes of the feed drive system (FDS) experience high variation with changing worktable positions. The predicted and measured natural frequencies for the first mode varied between 409 Hz and 372 Hz, with a variation rate of 9.98%. Similarly, the fourth mode had a natural frequency range of 321 Hz–298 Hz, with a variation rate of 7.1%. The data presented in Figure 7a indicate that the most significant variation occurred in the first mode, while less variation was observed in the third and second modes. This implies that changes in the worktable position will not have a substantial impact on the model caused by the rotational vibration of the coupling ball-screw–rotor or ball-screw–bearing.

When studying the impact of changing the worktable mass on the dynamics of the TBSFS, as indicated in Figure 8a and Tables 4 and 5, it emerged that the natural frequencies exhibit greater variations in the second and third modes of the FDS compared to the first and fourth modes in response to an increase in worktable mass. The predicted–measured values for the second mode vary between 302 Hz and 260 Hz, with a variation rate of 16%, while those for the third one were between 225 Hz and 202 Hz, with a change rate of 11%.
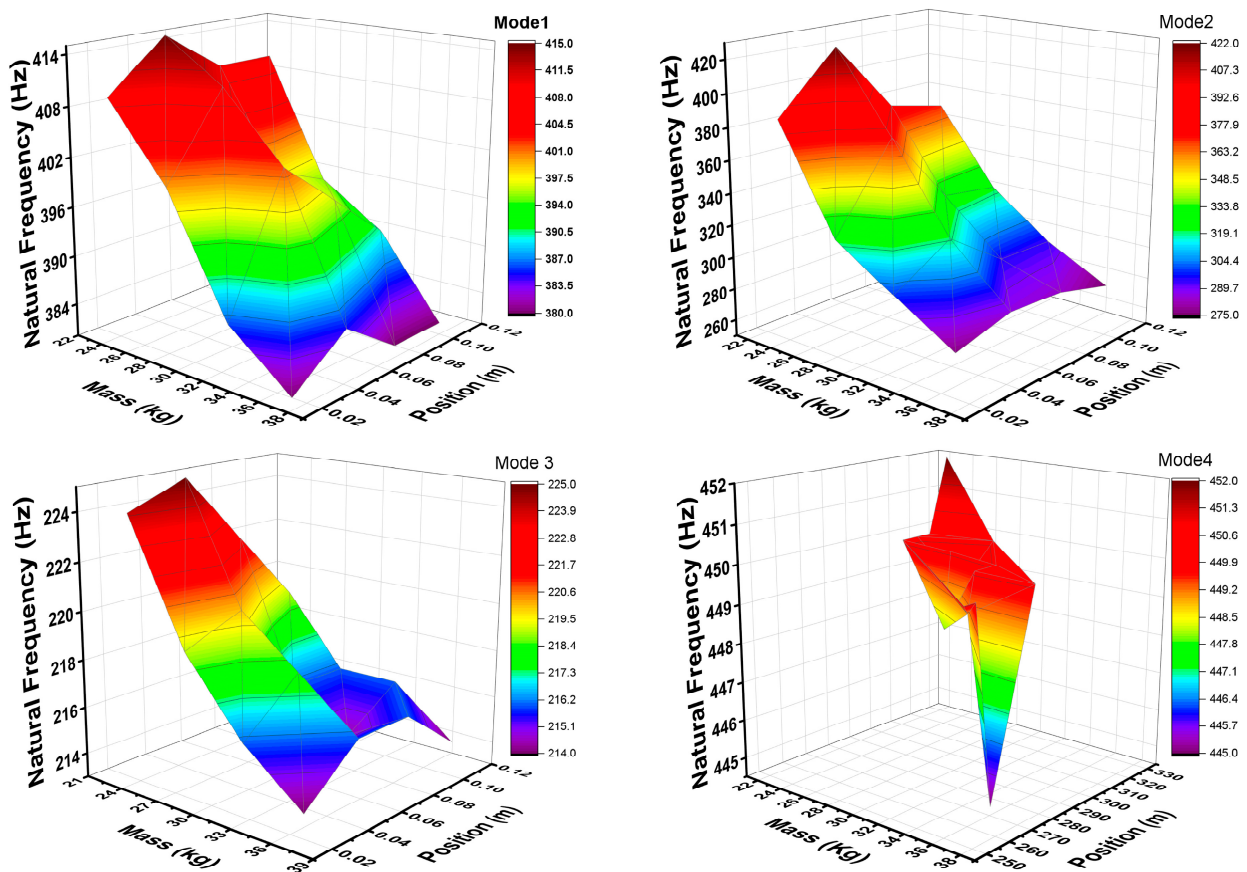
Figure 9. The impact of dual factors on the natural frequency of the system.

When analyzing the impact of changing the worktable position on the entire system, as shown in Figure 7b, considering their related magnitude, we found that the fourth mode has a high magnitude of 0.49 m/N at the first position with a natural frequency of 298 Hz. In addition, this mode consistently shows higher magnitudes compared to the other modes, implying that changes in the worktable position will highly affect the mode caused by the rotation vibration of the ball screw itself. The same process was adopted to address the impact of changes in worktable mass on the entire system; as shown in Figure 8b, it was found that the third mode possesses a high magnitude of 1 m/N with a natural frequency of 225 at the initial mass. It also consistently shows higher magnitudes compared to the other modes, which means that changes in worktable mass will highly affect the rotational vibration between ball screws and rotors.

Furthermore, when examining the impact of both position and mass simultaneously, as depicted in Table 6 and Figure 9, a significant variation rate was observed in the second mode (9.5%) and fourth mode (7.75%), while it was rarely observed in the first mode (2%) and third mode (1.76%). Figure 9 also shows that the second and third modes are influenced by changes in the worktable mass, while the first and fourth modes vary in line with changing worktable positions.

Considering the above discussion, it has been determined that a change in the position of the worktable significantly affects the mode attributed to the rotational and axial vibrations of the ball screws themselves (mode 4 and mode 1). The variation in worktable mass has a significant impact on the model caused by the axial vibration of the coupling ball-screw–bearing (mode 2). The proposed method reliably achieves performance variances between experimental and theoretical natural frequencies below 5%. This indicates potential enhancements in the modeling and analysis of TBSDM dynamics, as well as the method's ability to handle the complexity of the TBSDM dynamic model.

5. Conclusions

This paper characterizes the impact of mass and position variations on the dynamic behaviors of the twin-ball-screw drive mechanism (TBSDM), which adopts the drive at the center of gravity (DCG) concept. This study used mathematical models obtained through receptance coupling substructure approaches to produce theoretical results. Experimental validation was conducted using the TBSDM of CNC grinding wheel machine tools. The following conclusions are reached after a thorough examination of the aforementioned points. When conducting experimental and theoretical analyses of the frequency response functions (FRFs) of the entire system, this study endeavor discovered that the variances between the theoretical and experimental natural frequencies were consistently below 5%. Hence, the receptance coupling method in this study shows enormous potential for significantly enhancing the accuracy and effectiveness of TBSDM dynamic modeling.

An analysis was conducted on the vibration modes of the TBSDM by examining the distribution of natural frequencies in four different modes. The first mode refers to the axial vibration of the two ball screws, while the second mode pertains to the axial vibration of the twin ball screws and bearings. The third mode involves the torsional vibration between the twin ball screws and motors. The final mode, which is the fourth one, relates to the torsional vibration of the twin ball screws themselves. The variation in worktable mass mainly influences the mode caused by axial vibration between the twin ball screws and bearings, with a change rate of 16%, and torsional vibration between the ball screw and rotor, with an 11% change rate, while the change in worktable position highly affects the axial and rotational vibrations of the ball screws themselves at change rates of 10% and 7.1%, respectively. Therefore, based on the aforementioned statement, this research has demonstrated that receptance coupling is one of the methods that are relevant to analyzing the dynamic characteristics of TBSDM tools since it provides the impact of dynamic factors (mass, position) not only on the entire system but also on each system substructure. Although adopting the receptance coupling method for the analysis of dynamic characteristics significantly improves the modeling of the TBSDM, it is crucial to acknowledge that the presented model exclusively includes viscous friction, hence resulting in a linear system, which is not the case in many real-world systems. In order words, the results presented here are primarily applicable to situations involving viscous friction. Therefore, future works will prioritize the integration of dry friction into the model to capture the full range of dynamic behaviors, including those that result from nonlinear frictional forces.

References

1. Lin, C.-J.; Lin, C.-H.; Wang, S.-H. Using Fuzzy Control for Feed Rate Scheduling of Computer Numerical Control Machine Tools. *Appl. Sci.* **2021**, *11*, 4701. [CrossRef]
2. Tajima, S.; Sencer, B. Real-time trajectory generation for dual-stage feed drive systems. *CIRP Ann.* **2023**, *72*, 317–320. [CrossRef]
3. Xu, M.; Cai, B.; Li, C.; Zhang, H.; Liu, Z.; He, D.; Zhang, Y. Dynamic characteristics and reliability analysis of ball screw feed system on a lathe. *Mech. Mach. Theory* **2020**, *150*, 103890. [CrossRef]
4. Zhang, H.; Zhao, W.; Du, C.; Liu, H.; Zhang, J. Dynamic modeling and analysis for gantry-type machine tools considering the effect of axis coupling force on the slider–guide joints' stiffness. *Proc. Inst. Mech. Eng. Part B J. Eng. Manuf.* **2016**, *230*, 2036–2046. [CrossRef]
5. Hu, M.; Lu, H.; Liu, Q.; Dai, J.; Wang, B.; Wang, S. Analysis of Dynamic Parameter for Gantry Mobile-Type Dual-Drive Machine. In Proceedings of the ASME 2022 17th International Manufacturing Science and Engineering Conference, West Lafayette, IN, USA, 27 June–1 July 2022.
6. Chantal, U.M.; Lu, H.; Liu, Q.; Jiang, T.; Hu, M.; Gaspard, G. Analysis of Dual-Driven Feed System Vibration Characteristics Based on Computer Numerical Control Machine Tools: A Systematic Review. *Symmetry* **2023**, *15*, 2012. [CrossRef]
7. Zhao, J.; Lin, M.; Song, X.; Guo, Q. Analysis of the precision sustainability of the preload double-nut ball screw with consideration of the raceway wear. *Proc. Inst. Mech. Eng. Part J J. Eng. Tribol.* **2019**, *234*, 1530–1546. [CrossRef]
8. Li, B.; Luo, B.; Mao, X.; Cai, H.; Peng, F.; Liu, H. A new approach to identifying the dynamic behavior of CNC machine tools with respect to different worktable feed speeds. *Int. J. Mach. Tools Manuf.* **2013**, *72*, 73–84. [CrossRef]
9. Mauro, S.; Pastorelli, S.; Johnston, E. Influence of controller parameters on the life of ball screw feed drives. *Adv. Mech. Eng.* **2015**, *7*, 1687814015599728. [CrossRef]
10. Huang, T.; Kang, Y.; Du, S.; Zhang, Q.; Luo, Z.; Tang, Q.; Yang, K. A survey of modeling and control in ball screw feed-drive system. *Int. J. Adv. Manuf. Technol.* **2022**, *121*, 2923–2946. [CrossRef]
11. Zhang, W.; Zhu, D.; Huang, Z.; Zhu, Y.; Zhu, J. Dynamic parameters identification of rolling joints based on the digital twin dynamic model of an assembled ball screw feed system. *Adv. Mech. Eng.* **2022**, *14*, 16878132221108491. [CrossRef]
12. Chen, R.; Yan, L.; Jiao, Z.; Shang, Y. Dynamic modeling and analysis of flexible H-type gantry stage. *J. Sound Vib.* **2019**, *439*, 144–155. [CrossRef]
13. Chan, T.C.; Ullah, A.; Roy, B.; Chang, S.L. Finite element analysis and structure optimization of a gantry-type high-precision machine tool. *Sci. Rep.* **2023**, *13*, 13006. [CrossRef] [PubMed]
14. Liu, Q.; Lu, H.; Zhang, X.; Zhang, Y.; Wang, Y.; Li, Z.; Duan, M. A method to improve position accuracy for the dual-drive feed machines by state-dependent friction compensation. *Proc. Inst. Mech. Eng. Part B J. Eng. Manuf.* **2022**, *236*, 1247–1267. [CrossRef]
15. Duan, M.; Lu, H.; Zhang, X.; Zhang, Y.; Li, Z.; Liu, Q. Dynamic Modeling and Experiment Research on Twin Ball Screw Feed System Considering the Joint Stiffness. *Symmetry* **2018**, *10*, 686. [CrossRef]
16. Dong, L.; Tang, W.J.M. Hybrid modeling and analysis of structural dynamic of a ball screw feed drive system. *Mechanika* **2013**, *19*, 316–323. [CrossRef]
17. Ealo, J.; Garitaonandia, I.; Fernandes, M.; Hernandez-Vazquez, J.; Muñoa, J. A practical study of joints in three-dimensional Inverse Receptance Coupling Substructure Analysis method in a horizontal milling machine. *Int. J. Mach. Tools Manuf.* **2018**, *128*, 41–51. [CrossRef]
18. Schmitz, T. Modal interactions for spindle, holders, and tools. *Procedia Manuf.* **2020**, *48*, 457–465. [CrossRef]
19. Li, F.; Jiang, Y.; Li, T.; Du, Y. An improved dynamic model of preloaded ball screw drives considering torque transmission and its application to frequency analysis. *Adv. Mech. Eng.* **2017**, *9*, 1687814017710580. [CrossRef]
20. Li, C.; Chen, Z.; Yao, B. Adaptive Robust Synchronization Control of a Dual-Linear-Motor-Driven Gantry With Rotational Dynamics and Accurate Online Parameter Estimation. *IEEE Trans. Ind. Inform.* **2018**, *14*, 3013–3022. [CrossRef]
21. Zheng, J.; Deng, X.; Yang, J.; Zhang, W.; Lin, X.; Jiang, S.; Yao, X.; Shen, H. Analysis of thermal characteristics with multi-physics coupling for the feed system of a precision CNC machine tool. *Bull. Pol. Acad. Sci. Tech. Sci.* **2024**, *72*, e148941. [CrossRef]
22. Schmitz, T.L.; Duncan, G.S. Three-Component Receptance Coupling Substructure Analysis for Tool Point Dynamics Prediction. *J. Manuf. Sci. Eng.* **2005**, *127*, 781–790. [CrossRef]
23. Kiran, K. A receptance coupling procedure considering frequency-dependent behavior of holder-tool contact dynamics. *J. Manuf. Process.* **2022**, *80*, 624–641. [CrossRef]
24. Honeycutt, A.; Schmitz, T. Receptance coupling model for variable dynamics in fixed-free thin rib machining. *Procedia Manuf.* **2018**, *26*, 173–180. [CrossRef]
25. Tian, F.; Li, X.; Huang, Z. Multi-Position Identification of Joint Parameters in Ball Screw Feed System Based on Response Coupling. *Teh. Vjesn.* **2020**, *27*, 1723–1732.
26. Iglesias, A.; Tunç, L.T.; Özsahin, O.; Franco, O.; Munoa, J.; Budak, E. Alternative experimental methods for machine tool dynamics identification: A review. *Mech. Syst. Signal Process.* **2022**, *170*, 108837. [CrossRef]
27. Ji, Y.; Bi, Q.; Zhang, S.; Wang, Y. A new receptance coupling substructure analysis methodology to predict tool tip dynamics. *Int. J. Mach. Tools Manuf.* **2018**, *126*, 18–26. [CrossRef]
28. Liu, H.; Lu, D.; Zhang, J.; Zhao, W. Receptance coupling of multi-subsystem connected via a wedge mechanism with application in the position-dependent dynamics of ballscrew drives. *J. Sound Vib.* **2016**, *376*, 166–181. [CrossRef]

29. Tian, F.; Li, X.; Huang, Z. Modeling and dynamic characteristic analysis of a ball screw feed drive system based on receptance coupling. *Teh. Vjesn.* **2021**, *28*, 1691–1700.

30. Schmitz, T.; Smith, K. *Mechanical Vibrations: Modeling and Measurement*; Springer Science and Business Media LLC: Dordrecht, The Netherlands, 2013. [CrossRef]

31. Sobra, J.; Vaimann, T.; Belahcen, A. Mechanical vibration analysis of induction machine under dynamic rotor eccentricity. In Proceedings of the 2016 17th International Scientific Conference on Electric Power Engineering (EPE), Prague, Czech Republic, 16–18 May 2016; pp. 1–4.